Article

Mechanochemical Synthesized CaO/ZnCo$_2$O$_4$ Nanocomposites for Biodiesel Production

Katabathini Narasimharao * , Mohamed Mokhtar M. Mostafa * , Zahra M. Al-Amshany and Wejdan Bajafar

Department of Chemistry, Faculty of Science, King Abdulaziz University, P.O. Box 80203, Jeddah 21589, Saudi Arabia
* Correspondence: nkatabathini@kau.edu.sa (K.N.); mmoustafa@kau.edu.sa (M.M.M.M.)

Abstract: Biodiesel has been recognized as an environmentally friendly, renewable alternative to fossil fuels. In this work, CaO/ZnCo$_2$O$_4$ nanocomposites were successfully synthesized via simple mechanochemical reaction between ZnCo$_2$O$_4$ and CaO powders by varying the CaO loading from 5 to 20 wt.%. The synthesized materials were found to be highly efficient heterogeneous catalysts for transesterification of tributyrin with methanol to produce biodiesel. The nanocomposite, which contained 20 wt.% CaO and 80 wt.% ZnCo$_2$O$_4$ (CaO/ZnCo$_2$O$_4$-20), exhibited superior and stable transesterification activity (98% conversion) under optimized reaction conditions (1:12 TBT to methanol molar ratio, 5 wt.% catalyst and 180 min. reaction time). The experimental results revealed that the reaction mechanism on the CaO/ZnCo$_2$O$_4$ composite followed pseudo first-order kinetics. The physicochemical characteristics of the synthesized nanocomposites were measured using X-ray diffraction (XRD), high resolution transmission electron microscopy (HRTEM), Fourier-transformed infrared spectroscopy (FTIR), X-ray photoelectron spectrometer (XPS), N$_2$-physisorption, and CO$_2$-temperature-programmed desorption (CO$_2$-TPD) techniques. The results indicated the existence of coalescence between the CaO and ZnCo$_2$O$_4$ particles, Additionally, the CaO/ZnCo$_2$O$_4$-20 catalyst was found to possess the greater number of highly basic sites and high porosity, which are the key factors affecting catalytic performance in transesterification reactions.

Keywords: CaO/ZnCo$_2$O$_4$; nanocomposite; mechanochemical synthesis; transesterification; biodiesel; kinetic studies

1. Introduction

Most of the energy consumed globally originates from fossil fuels such as coal, petroleum, and natural gas. Indeed, fossil fuels currently account for around 86% of total energy usage [1,2]. Nonetheless, these sources are limited and may run out in the next century [3]. The combustion of fossil fuels emits air pollutants and toxic gases such as SO$_x$, NO$_x$, and CO$_x$, volatile organic compounds, and heavy metals which can cause dangerous diseases. In addition, CO$_2$ emissions are one of the most significant direct contributors to global warming [4]. As such, many researchers and decision-makers across the world have started to seek alternative and clean energy sources. Alternative energy sources should be cost-effective, technically feasible, simple to store and transport, environmentally friendly, and widely available to the public [5–10].

In the last two decades, biodiesel has emerged as a promising renewable alternative to petroleum diesel [11]. Biodiesel is a general term for several ester-based oxygenated fuels derived from renewable sources, such as vegetable oils and animal fats [12–14]. Biodiesel resembles petroleum diesel in terms of its physical, chemical, and combustion properties, but it is sulphur-free, making it a cleaner-burning fuel [15–17]. Biodiesel can be obtained from the transesterification of vegetable oils or animal fats with alcohols [18]. The choice of feedstocks for biodiesel production is a key factor in making it a viable alternative to petroleum-based diesel. Plenty of oils from plants and animal fat have been used as feedstocks for the synthesis of biodiesel. Tributyrin (TBT), also known as

glyceryl tributyrate, with chemical formula $C_{15}H_{26}O_6$, is a short-chain aliphatic ester. TBT is naturally found in animal fats, vegetable oils, dairy products, etc., and is mainly used in the processing of margarine [19]. Synthetically, TBT can be produced by reacting glycerin and butyryl chloride with an organic base. In this research, TBT is used as a raw material to produce biodiesel. The presence of a catalyst in the transesterification process is essential to enhance the rate of reaction and the yield. For industrial biodiesel production, homogeneous catalysts are used; however this approach suffers from significant drawbacks, such as high production costs due to the need to separate of K^+ and Na^+ ions and glycerol [20]. The utilization of enzyme catalysts has significant advantages, but it is currently not feasible due to the relatively high cost and unstable behaviour of enzymes.

The utilization of an efficient heterogeneous catalyst could be advantageous because, contrary to homogeneous catalysts, no separation procedures are required. In most cases, the catalysts can be reused and recycled for an extended time, allowing for continuous operation on a large scale [21]. For biodiesel production, a variety of heterogeneous basic catalysts, such as alkaline earth metal oxides, alkali metals exchanged zeolites, and hydrotalcites, has been studied. Because of their high basicity, alkaline earth metal oxides offer high biodiesel yields [22]. Li et al. [23] utilized Li/NaY zeolite catalysts for biodiesel production and observed yields of 98.6%. The spent catalyst characterization results showed that the catalyst has excellent stability with a moderate regenerative capacity. Sulaiman et al. [24] studied the conversion of refined and used cooking oils into safer and low toxicity biodiesel via base-catalysed transesterification. Alumina supported magnesium, calcium, strontium, and barium oxide-based catalysts with iron as a dopant offered a maximum biodiesel yield of 84.0%.

Several studies have indicated that calcium oxide (CaO) is a promising catalyst for the transesterification for biodiesel production because of its low cost, ease of production from natural and waste raw materials, high catalytic activity and lack of significant negative environmental effects [25]. Sai Bharadwaj et al. [26] synthesized biodiesel from non-edible rubber seed oil using CaO prepared from eggshells. A conversion rate of 99.7% of oil to biodiesel was obtained with a 12:1 methanol to oil molar ratio and 4 wt.% catalyst in 3 h. However, the leaching of Ca^{2+} is a major drawback of the use of CaO as a catalyst; additionally, it is sensitive to free fatty acids (FFAs), as the leached Ca^{2+} species react with FFAs to form undesired soap products [27]. Several researchers have attempted to substitute CaO for another metal oxide to improve the stability of the process. Yu et al. [28] reported the production of biodiesel over $CaO–CeO_2$ catalysts by the transesterification of Pistacia chinensis oil, obtaining a yield of 91% at 110 °C.

In recent years, spinel oxides have emerged as an alternative to conventional heterogeneous supports due to their unique crystal structure and chemical and thermal stability [29]. These compounds are typically expressed with the general formula of AB_2O_4 [30]. The co-precipitation method is the most common method used for the preparation of spinel nanomaterials, but this method is laborious. Liu et al. [31] synthesized $CaO/MgFe_2O_4$ catalysts by co-precipitation and used it for to produce biodiesel from soybean oil. In traditional methods, the synthesis of catalysts generally involves multi-step processes, heating, and/or the addition of expensive and hazardous reagents. By contrast, the mechanochemical method can overcome these drawbacks by using simple grinding or milling under optimized conditions. In mechanochemical reactions, the reactants are broken apart by mechanical force, which leads to an amorphous mixture of all reagents and a higher surface for the reaction to take place on. The effect of the mechanical action can reduce the particle size and create active sites by generating new active surfaces which can connect to other particles, thereby increasing the chemical activity of the materials [32]. In the present study, we synthesized low-cost heterogeneous $CaO/ZnCo_2O_4$ nanocomposites by a mechanochemical synthesis method and used the materials as catalysts for the transesterification of tributyrin with methanol. The influence of different reaction conditions, such as the oil to methanol molar ratio, reaction time and temperature, on the performance of the catalysts was also studied. The synthesized materials were analyzed using X-ray diffraction

(XRD), high resolution transmission electron microscopy (HRTEM), Fourier-transform infrared spectroscopy (FT-IR), N_2-physisorption, X-ray photoelectron spectrometer (XPS) and CO_2-temperature-programmed desorption (CO_2-TPD) techniques. The correlation between the catalytic performance and the physicochemical characteristics of the catalysts was also studied.

2. Results and Discussion

2.1. XRD

XRD analysis was used for phase detection and to investigate the crystal structure of the synthesized $ZnCo_2O_4$, CaO and $CaO/ZnCo_2O_4$ composite catalysts; the obtained patterns are shown in Figure 1. The bare $ZnCo_2O_4$ sample exhibited reflections at 19°, 31.6°, 37.4° and 44.6°, corresponding to the (110), (220), (310), (400), (511) and (440) planes of cubic structure of the $ZnCo_2O_4$ spinel [JCPDS file#00-001-1149]. No other reflections were observed for any other crystal phase, indicating the high purity of the synthesized $ZnCo_2O_4$ material.
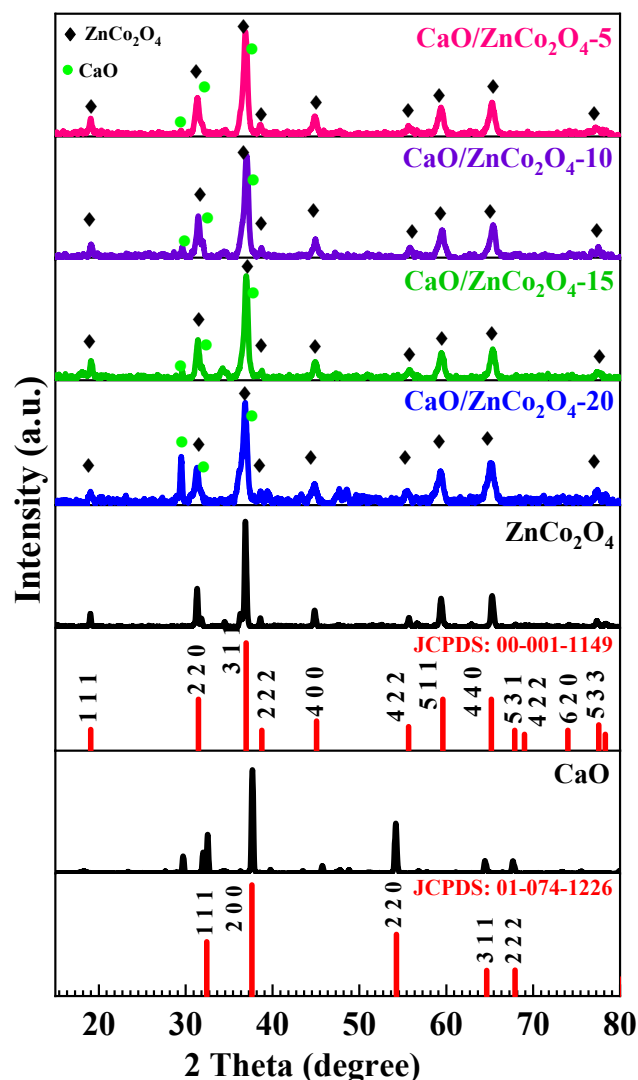

Figure 1. XRD patterns of CaO, $ZnCo_2O_4$ and $CaO/ZnCo_2O_4$ composite samples.

The XRD pattern of the synthesized bare CaO sample showed all reflections due to the presence of a cubic CaO structure [JCPDS file#01-074-1226]. The $CaO/ZnCo_2O_4$ composite samples featured the characteristic reflections of both $ZnCo_2O_4$ and CaO crystal phases. It is interesting to note that reflections due to the crystalline CaO phase were observed even

composite with low CaO loading (5 wt.%); this was probably due to the high crystallinity of CaO. The intensity of the CaO reflections increased with an increase of CaO loading from 5 to 20 wt.%. The average crystallite sizes of both the $ZnCo_2O_4$ and CaO phases for all the synthesized materials were calculated using the Scherrer equation. Table 1 illustrates the calculated crystallite sizes of the $ZnCo_2O_4$ and CaO phases for the synthesized samples. It is clear that the crystallite size of CaO is large compared to that of $ZnCo_2O_4$; interestingly, the crystallite sizes of both CaO and $ZnCo_2O_4$ were slightly decreased in the composites, probably due to the mechanical grinding.

Table 1. The crystallite sizes of $ZnCo_2O_4$ and CaO phases for the synthesized samples.

Catalyst	Crystallite Size (nm)	
	$ZnCo_2O_4$	CaO
CaO	-	38
$ZnCo_2O_4$	27	-
CaO/$ZnCo_2O_4$-5	16	30
CaO/$ZnCo_2O_4$-10	14	28
CaO/$ZnCo_2O_4$-15	12	25
CaO/$ZnCo_2O_4$-20	12	25

2.2. HRTEM Analysis

The HRTEM images and particle size distribution of the synthesized catalysts are shown in Figure 2. The images of bare $ZnCo_2O_4$, CaO and CaO/$ZnCo_2O_4$-20 samples consist of isolated and agglomerated spherical nanoparticles. The average particle size of CaO and $ZnCo_2O_4$ samples is around 31 nm and 28 nm, respectively. On other hand, the particle size of the CaO/$ZnCo_2O_4$-20 sample was around 21 nm, which is less than that of the parent compounds of the nanocomposites, as shown in the histograms (Figure 2), which is in accordance with the crystallite sizes determined from XRD results. The HRTEM images of the CaO and $ZnCo_2O_4$ samples shows the lattice fringes with a distance of 0.24 nm, corresponding to the (200) plane of the CaO phase, and 0.286 nm, which was attributed to the *d*-spacing of the (200) plane of the spinel structure of $ZnCo_2O_4$ [33,34]. The HRTEM image of the mechanochemically synthesized CaO/$ZnCo_2O_4$-20 composite sample showed the presence of lattice fringes for both $ZnCo_2O_4$ and CaO particles. The image of the composite sample clearly shows existence of interface (marked with red color eclipse) between the particles revealing coalescence between the CaO and $ZnCo_2O_4$ particles. This observation is indicating that the two crystalline phases grown together due to vigorous milling and thermal treatment procedures adapted during the synthesis of CaO/$ZnCo_2O_4$ composite.

2.3. FT-IR

FT-IR spectroscopy was employed to investigate the functional groups present in the synthesized samples. Figure 3 shows the FT-IR spectra for the synthesized catalysts obtained at room temperature. The bare $ZnCo_2O_4$ has a characteristic band in the region of 3440 to 3615 cm^{-1}, which could be attributed to H-O-H stretching vibrations, indicating the presence of water molecules. The intense IR bands observed at 1628 cm^{-1} and at 1387 cm^{-1} were assigned to CO_3^{-2} groups [35]. The strong absorption bands at 666 and 566 cm^{-1} were due to the intrinsic stretching vibrations of Zn-O at tetrahedral lattice sites and Co-O at octahedral sites, respectively. The observed results indicated the successful formation of cubic structured $ZnCo_2O_4$, which is in concurrence with the XRD results [36].
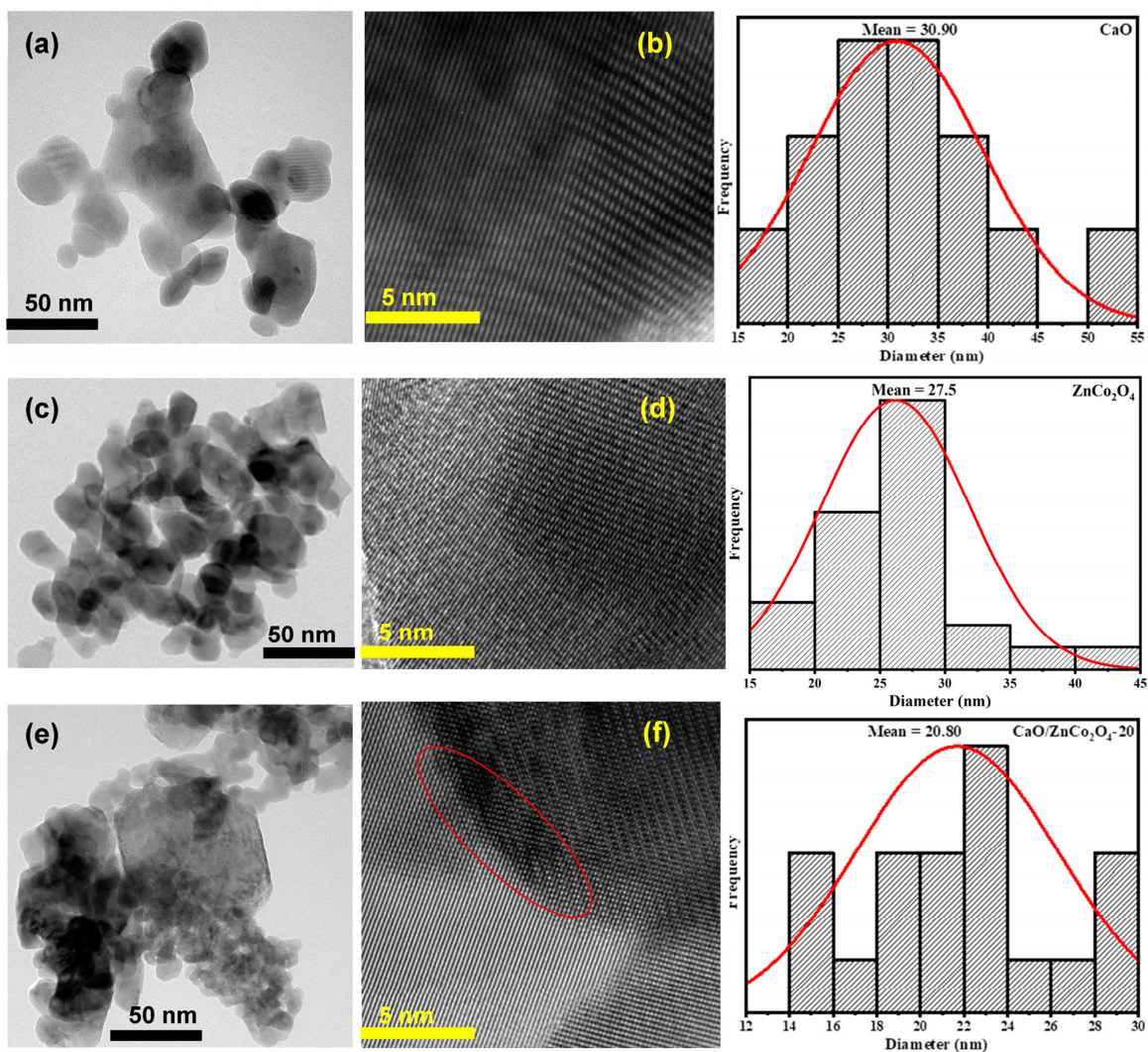
Figure 2. HRTEM images and particle size distribution patterns of the synthesized CaO (**a**,**b**), $ZnCo_2O_4$ (**c**,**d**) and $CaO/ZnCo_2O_4$-20 (**e**,**f**).
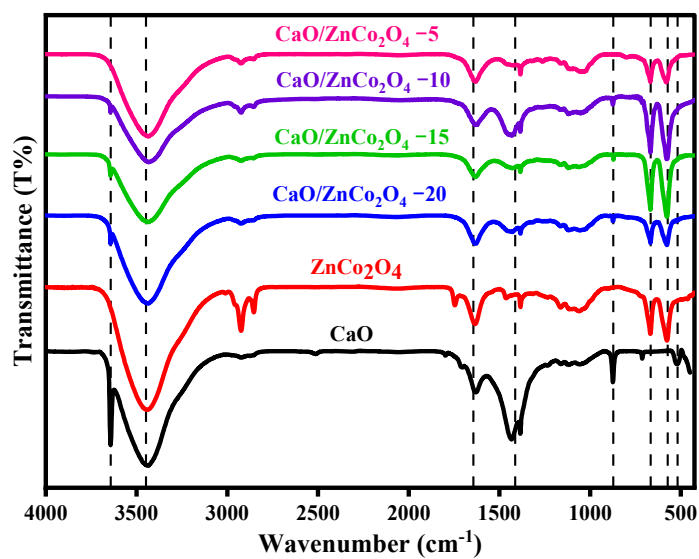

Figure 3. FT-IR spectra of the synthesized samples.

The spectrum of the bare CaO sample displayed an absorption band at 3647 cm^{-1}, corresponding to the bending vibration modes of the OH groups from the remaining hydroxide or from H$_2$O molecules on the external surface of the sample, likely present as a result of handling the specimen before recording the spectra [37]. The broad band around 1400–1500 cm^{-1}, as well as the weak band at 873 cm^{-1}, is characteristic of C-O bonds related to the carbonation of CaO [38]. The characteristic IR band at 520 cm^{-1} for CaO signified the presence of a Ca-O functional group. The spectra of the CaO/ZnCo$_2$O$_4$ nanocomposite samples showed similar absorption bands to those of the bare CaO and bare ZnCo$_2$O$_4$ samples, indicating the presence of functional groups in both the CaO and ZnCo$_2$O$_4$ phases.

2.4. N$_2$ Gas Physisorption Measurements

Figure 4 illustrates the N$_2$ gas adsorption/desorption isotherms of the samples. All the isotherms could be identified as type IV, as per the IUPAC classification [39]. The hysteresis loops in the isotherms indicated the mesoporous nature of all catalysts. The presence of H3-type hysteresis loops in the isotherms indicated that the catalysts possessed slit pores which formed due to the aggregation of sheet like particles [40]. Table 2 displays the calculated textural properties, such as the BET surface area (S$_{BET}$), micropore surface area (S$_{micro}$), mesopore surface area (S$_{meso}$), total pore volume (V$_{total}$), micropore volume (V$_{micro}$) and mesopore volume (V$_{meso}$) for representative samples. The highly crystalline CaO sample exhibited a low BET-surface area (6.0 m^2/g), while the ZnCo$_2$O$_4$ sample possessed a surface area of 32 m^2/g, which is high for a spinel structured sample. Interestingly, the composite samples showed surface areas less than that of ZnCo$_2$O$_4$ but higher than that of CaO. For instance, CaO/ZnCo$_2$O$_4$-20 exhibited a surface area of 23 m^2/g, possibly due to presence of CaO particles in the pore channels of ZnCo$_2$O$_4$. A pore size distribution analysis was carried out using NLDFT method. The pore size distribution patterns indicated that the samples had multimodal pores in the micro, meso and macro size ranges [41]. The pore volume and average pore size properties of the composite samples also showed a similar trend to that of the surface area.
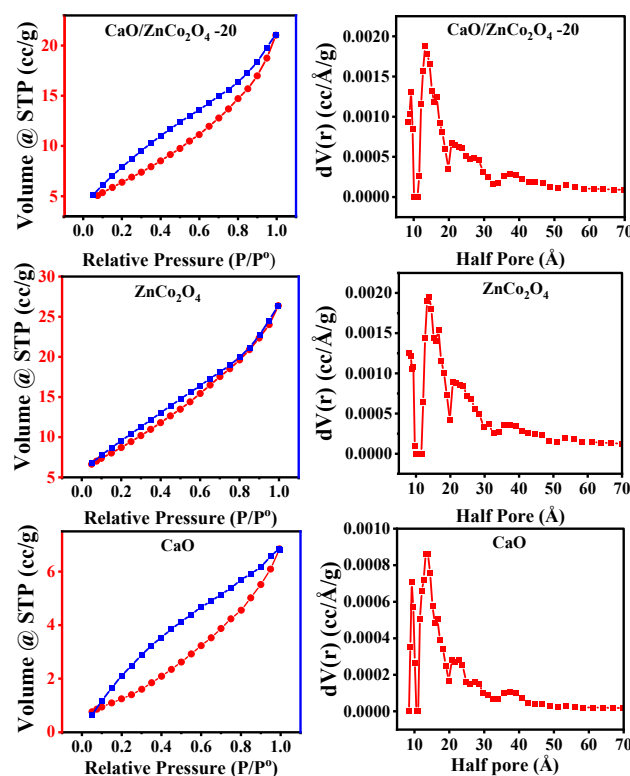

Figure 4. N$_2$ gas adsorption–desorption isotherms and pore size distribution patterns of the samples.

Table 2. Textural properties of different catalysts from N_2 gas physisorption.

Sample	S_{BET} (m²/g)	S_{micro} (m²/g)	S_{meso} (m²/g)	V_{total} (cc/g)	V_{micro} (cc/g)	V_{meso} (cc/g)	Average Pore Size (nm)
CaO/ZnCo₂O₄-20	23.0	7.0	14	0.033	0.006	0.023	3.0
ZnCo₂O₄	32.0	12.0	16	0.041	0.007	0.027	3.0
CaO	6.0	0.0	5.8	0.01	0.00	0.01	4.0

2.5. XPS

The surface elemental composition and oxidation state of the elements presented in the synthesized catalysts were analyzed using XPS analysis. The deconvoluted XPS spectra of the samples are shown in Figure 5. For the sake of clarity, only *2p*$_{3/2}$ components for the Zn *2p* and Co *2p* spectra are presented in the figure. The Zn *2p*$_{3/2}$ component present in the synthesized ZnCo₂O₄ catalyst showed three deconvoluted Zn *2p*$_{3/2}$ peaks at 1020 eV, 1021.2 eV and 1022.2 eV. The peaks observed at about 1020 eV and 1021.2 eV could be attributed to the Zn-O bonds in the ZnCo₂O₄, while the other peak at 1022.2 eV could be assigned to Zn(OH)₂ species [42]. Interestingly, the CaO-ZnCo₂O₄ composite sample only exhibited two peaks at 1021.1 eV and 1022 eV, corresponding to Zn-O and Zn(OH)₂ species, respectively.
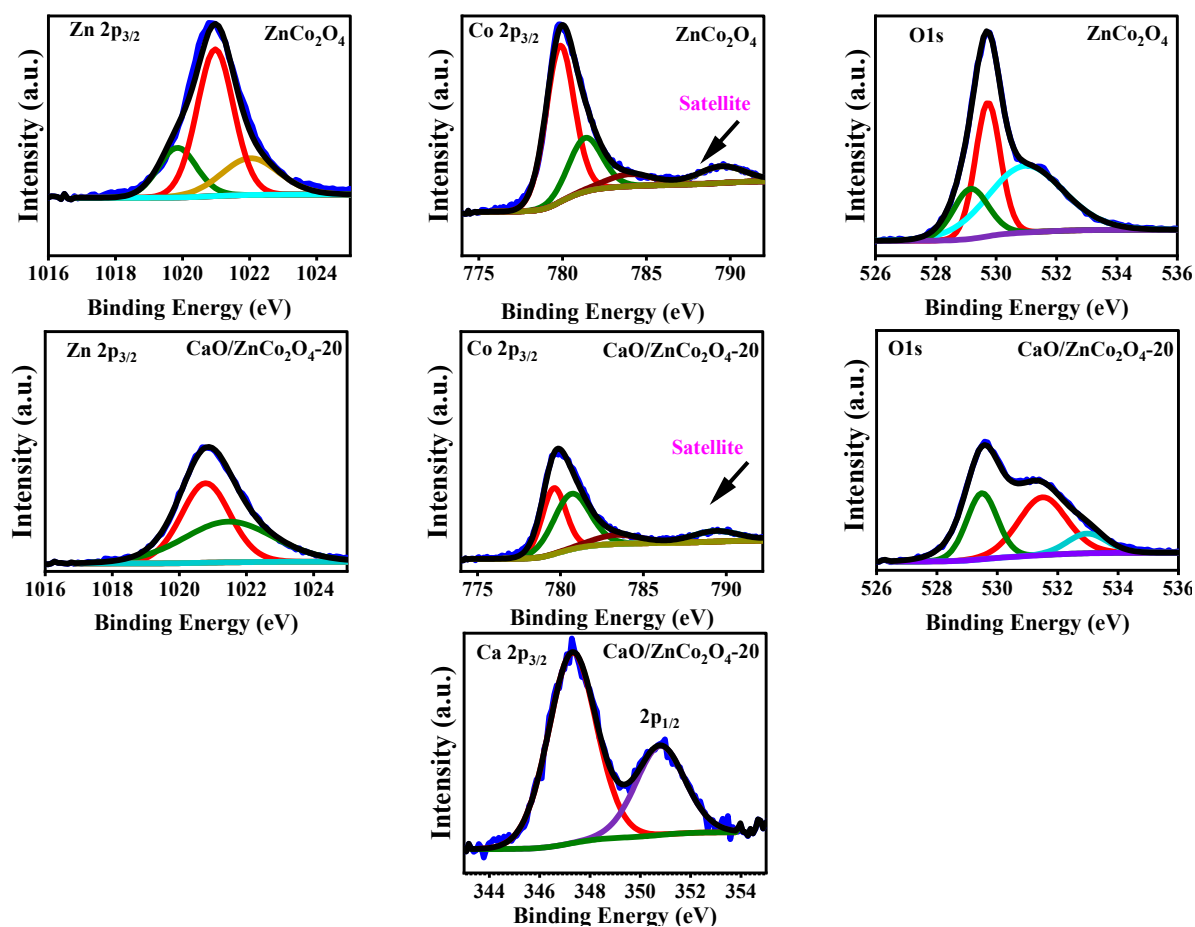
Figure 5. Deconvoluted XPS spectra of the ZnCo₂O₄ and CaO/ZnCo₂O₄-20 samples.

The Co *2p*$_{3/2}$ peak in the ZnCo₂O₄ and CaO/ZnCo₂O₄ composite samples could be fitted into two peaks. The fitted peaks at 780.0 eV and 781.6 eV could be assigned to Co³⁺, and Co²⁺ species. It has been reported that bulk cobalt oxides such as Co₃O₄ possess

mixed oxidation states of Co^{2+} and Co^{3+} and are expected to show satellite features due to both Co^{2+} and Co^{3+} states. Both spectra showed a satellite peak at around 786 eV for the Co^{2+} species [43]. Moreover, the integral area corresponding to the Co^{3+} peak was much larger than that of the Co^{2+} peak, which revealed that the main oxidation state of Co in the three spinel samples was Co^{3+} [44]. These observations indicated that the surface of the synthesized samples had a composition containing Co^{3+} and Zn^{2+}. The O *1s* spectra of the two samples could be fitted into three peaks. The peak at 529.5 eV matched the oxygen in the crystal lattice that bonded with metal ions, the peak at 531.5 eV corresponded to the oxygen of the OH^- groups and the peak at 533.3 eV corresponded to the oxygen of the physically adsorbed H_2O molecules [45]. The Ca *2p* peak of $CaO/ZnCo_2O_4$ composite sample showed the spin-orbit doublet for Ca $2p_{3/2}$ and Ca $2p_{1/2}$ components. A reasonably well-defined valley between the Ca $2p_{3/2}$ and Ca $2p_{1/2}$ existed in the spectra of the samples, indicating that the samples did not possess many physically adsorbed carbonate or hydroxyl groups due to calcination. The BE of the Ca $2p_{3/2}$ and Ca $2p_{1/2}$ components appeared at 347.4 eV and 351.1 eV and could be attributed to the Ca^{2+} oxidation state [46]. The XRD, TEM and XPS results clearly indicated the formation of a $CaO/ZnCo_2O_4$ composite by the mechanochemical synthesis method.

2.6. CO_2-TPD

The basicity of the synthesized catalysts was evaluated using CO_2-temperature-programmed desorption. Figure 6 illustrates the deconvoluted CO_2-TPD profiles of three representative catalysts. A broad desorption peak in the temperature range of 500–680 °C was observed for the bare CaO sample. On other hand, the bare $ZnCo_2O_4$ sample exhibited one small desorption peak centered at 620 °C and a major desorption peak at 720 °C. It is interesting that the $CaO/ZnCo_2O_4$-20 sample showed the presence of three desorption peaks at 750 °C, 800 °C and 908 °C. The CO_2 desorption temperature of all the samples were found to be higher than 400 °C, suggesting the high strength of the CO_2 adsorption sites, indicating that all the catalysts possessed strong basic sites [47]. CO_2 uptake was also quantified; the results indicated that the $CaO/ZnCo_2O_4$-20 catalyst uptake (1276 µmol/g, Table 3) was higher than those of both $ZnCo_2O_4$ (677 µmol/g) and CaO (904 µmol/g). The improved basicity of the $CaO/ZnCo_2O_4$-20 composite sample was due to the synergetic effect between $ZnCo_2O_4$ and CaO. Furthermore, it was observed that the $CaO/ZnCo_2O_4$-20 catalyst exhibited CO_2 desorption peaks at high temperatures compared to bare $ZnCo_2O_4$ and CaO, which indicates that the composite sample possessed more strong basic sites than its parent oxides. The observed characterization results indicated that the $CaO/ZnCo_2O_4$ composite samples could offer high catalytic activity for a base catalyzed transesterification process [47].

Table 3. Data obtained from CO_2-TPD analysis of CaO, $ZnCo_2O_4$ and $CaO/ZnCo_2O_4$-20 samples.

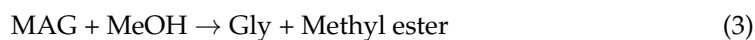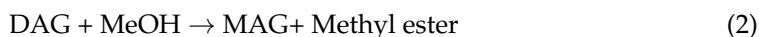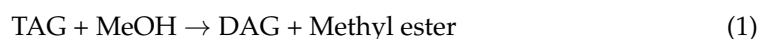| Catalyst	Temp. (°C)	CO_2 Uptake (µmol/g)	Total CO_2 Uptake (µmol/g)
$CaO/ZnCo_2O_4$-20	750 800 908	251 539 486	1276
$ZnCo_2O_4$	620 720	152 545	677
CaO	638	904	904

Figure 6. Deconvoluted CO_2-TPD patterns of the CaO, $ZnCo_2O_4$ and $CaO/ZnCo_2O_4$-20 samples.

2.7. Catalytic Activity

The synthesized samples were used as catalysts for the transesterification of tributyrin with methanol to produce biodiesel (methyl esters). The transesterification of tributyrin with methanol produces methyl esters and glycerin via three different elementary reactions (Equations (1)–(3)). The reaction between triglycerides (TAG) and methanol (MeOH) yields methyl-esters and diglycerides (DAG) in the first step. The reaction between diglycerides and methanol in the next step produces methyl esters and monoglycerides (MAG). In the final step, the monoglycerides are converted to methyl-esters and glycerin (Gly).

$$TAG + MeOH \rightarrow DAG + Methyl\ ester \tag{1}$$

$$DAG + MeOH \rightarrow MAG + Methyl\ ester \tag{2}$$

$$MAG + MeOH \rightarrow Gly + Methyl\ ester \tag{3}$$

A ^1H NMR and ^{13}C NMR analysis was performed to characterize the synthesized biodiesel (Figures S1 and S2). The ^1H NMR of the purified separated sample showed two triplet signals at δ 0.82 and 2.24 ppm due to CH_3 and CH_2 groups, respectively, a multiplet signal at 1.42–1.54 due to CH_2 groups, and a singlet signal at δ 3.71 ppm due to OCH_3 groups, which is in complete agreement with the structure of methyl butyrate.

To optimize the reaction conditions in order to achieve the highest catalytic activity, activity measurements over catalysts were carried by varying parameters such as the methanol/TBT molar ratio, reaction temperature and reaction time. Preliminarily, the influence of the reaction time on the conversion of TBT and yield of biodiesel over the synthesized catalysts was studied at 80 °C; the results are shown in Figure 7a. As the reaction time increased to 180 min, the TBT conversion levels increased gradually (not reaching 100% conversion) with the $ZnCo_2O_4$, $CaO/ZnCo_2O_4$-5, $CaO/ZnCo_2O_4$-10 and $CaO/ZnCo_2O_4$-15 samples. The conversion levels did not change significantly as the reaction time was increased 60 min, indicating that the equilibrium had been reached within 60 min. With a further increase of the reaction time, the conversion levels slightly increased and reached a maximum of 20% for $CaO/ZnCo_2O_4$-10 and 80% for $CaO/ZnCo_2O_4$-15.

This was mainly due to the presence of a limited number of active sites on the surface of these catalysts. Moreover, transesterification progresses as a stepwise reaction of the triglycerides, resulting in the formation of intermediate diglycerides and monoglycerides, which are then converted into biodiesel and glycerin [48]. However, in case of bare CaO, and the CaO/ZnCo2O4-20 samples, the TBT conversion levels increased drastically within 30 min. and reached 100% in just 60 min. This was due to the presence of a greater number of active sites in these two catalysts, resulting high conversion levels in the case of CaO/ZnCo2O4-20 and the bare CaO catalyst. Although bulk CaO offered high catalytic activity, its recyclability is difficult; this difficulty was not observed in the case of the CaO/ZnCo2O4-20 composite.
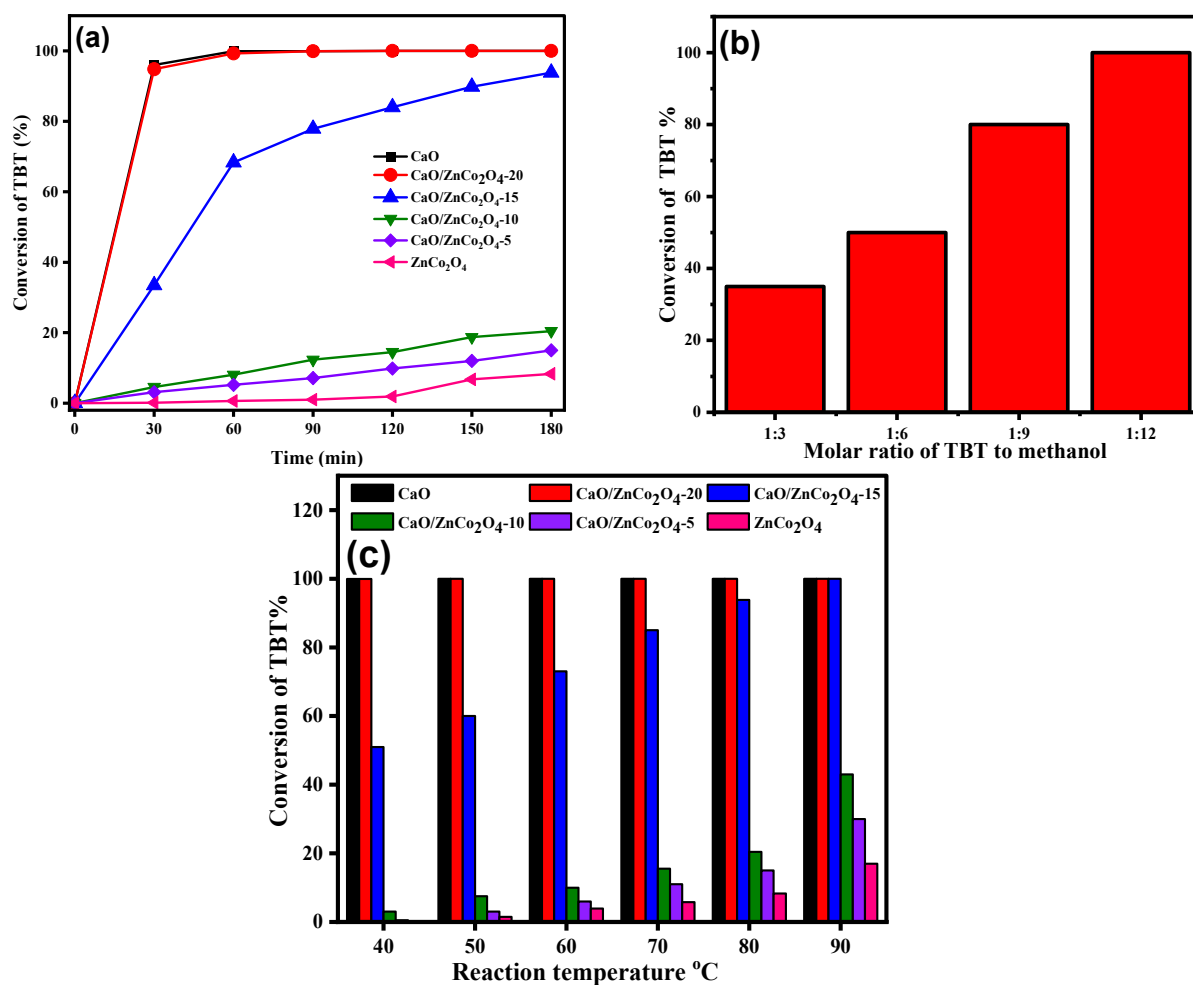

Figure 7. (**a**) Influence of reaction time on the TBT conversion over all synthesized catalysts. (Reaction conditions: 80 °C temperature, 1:12 TBT to methanol molar ratio, 5 wt.% catalyst and 180 min reaction time.) (**b**) Influence of different TBT to methanol molar ratio on TBT conversion (Reaction conditions: 80 °C temperature, 5 wt.% catalyst and 180 min reaction time), (**c**) Influence of reaction temperature on the TBT conversion over all synthesized catalysts. (Reaction conditions: 1:12 TBT to methanol molar ratio, 5 wt.% catalyst and 180 min reaction time.)

The influence of the molar ratio of TBT and methanol on biodiesel yield is shown in Figure 7b. It is well known that the transesterification reaction is reversible, and a higher molar ratio is required to shift the reaction equilibrium to the right. Figure 7b shows that as the amount of methanol increased, the biodiesel production increased, with the maximum biodiesel production of 100% being achieved with a 1:12 oil-to-methanol molar ratio over the CaO/ZnCo2O4-20 catalyst. This was possibly due to the formation more methoxy species on the surface of the catalyst which shifted the reaction equilibrium to the right to

achieve maximum biodiesel production [49]. The transesterification reaction was catalyzed by synthesized $ZnCo_2O_4$, CaO, and the $CaO/ZnCo_2O_4$ catalysts and was carried out in the temperature range of 40–90 °C to assess the effect of the reaction temperature on the conversion of TBT to biodiesel (see Figure 7c). The obtained results clearly indicate that CaO and $CaO/ZnCo_2O_4$-20 samples are efficient catalysts for the transesterification of TBT compared to other samples due to the presence of large numbers of basic sites, as shown in the CO_2-TPD analysis. The conversion of TBT was enhanced with an increase in the reaction temperature in all catalyst samples. The possible reason for this is that increasing the temperature lowered the viscosity of TBT, enhanced the collision rate of molecules and increased the effective collisions between the molecules, thereby leading to a higher conversion of TBT to biodiesel [50].

2.8. Selectivity

As shown in Equations (1)–(3), it was possible to form different glycerides along with methyl ester; therefore, the determination of selectivities for different products is important. It was observed that the selectivity to methyl butyrate was between 97% and 99% for the highly active $CaO/ZnCo_2O_4$-20 catalyst (Figure 8). There was no significant change in the selectivity to methyl butyrate when the reaction temperature was changed from 40 °C to 90 °C. This was possibly due to fact that the $CaO/ZnCo_2O_4$-20 catalyst possessed relatively large surface area, pore diameter and highly active basic sites for transesterification, which enhanced the diffusion of the reactant and product molecules.
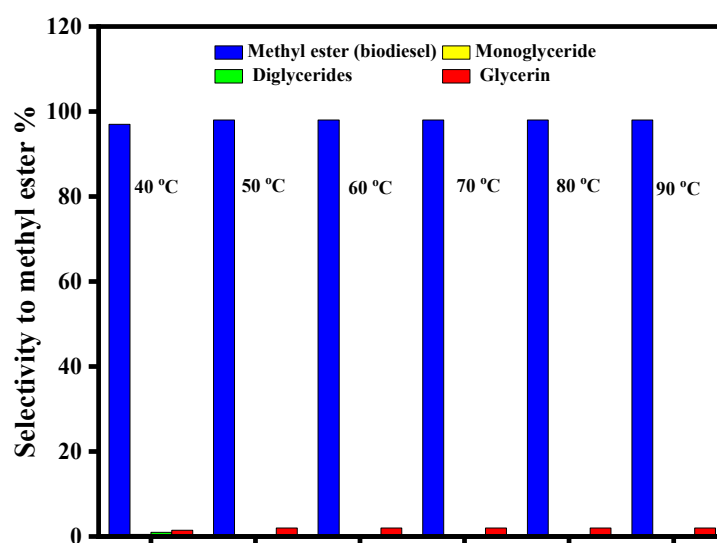

Figure 8. Selectivities of transesterification products over $CaO/ZnCo_2O_4$-20 catalyst at different reaction temperatures.

2.9. Reusability

Experiments were carried out to test the reusability of the $CaO/ZnCo_2O_4$-20 and CaO catalysts for biodiesel production; the results are shown in Figure 9. After each reaction, the $CaO/ZnCo_2O_4$-20 and CaO catalysts were separated from the reaction mixture using centrifugation, washed with methanol and dried fully for reutilization. It was observed that the conversion of TBT decreased sharply over the bare CaO catalyst and achieved less than 50% conversion in the fifth cycle. The deactivation of the CaO catalyst may have been caused by three possible factors. The first is CaO leaching into the reaction mixture due to the reaction with methanol to form calcium methoxide; the second is CaO surface poisoning due to the adsorption of fatty acid and glycerol molecules; and third is structure collapse [49]. The $CaO/ZnCo_2O_4$-20 catalyst exhibited better catalytic performance compared with bare CaO, although the conversion of TBT dropped to only 10% after the fifth run probably due to a loss of catalyst mass during the reuse procedure. Therefore, the

CaO/ZnCo$_2$O$_4$-20 catalyst was found to be economically suitable for industrial application from a practical point of view.
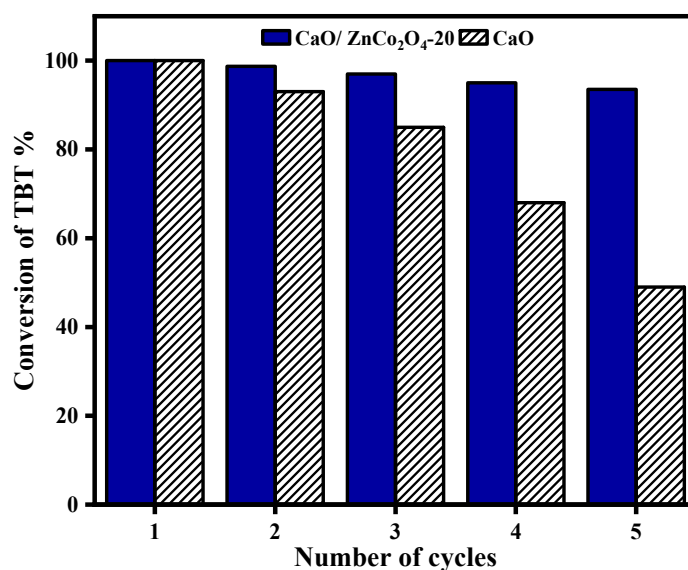

Figure 9. Reusability of CaO/ZnCo$_2$O$_4$-20 and CaO catalysts. (Reaction conditions: 80 °C temperature, 1:12 TBT to methanol molar ratio, 5 wt.% catalyst and 180 min reaction time).

2.10. Kinetic Studies

The optimized reaction conditions were used to perform kinetic studies of the transesterification of tributyrin with methanol over the synthesized catalysts. The reaction requires a stoichiometric amount of 3 moles of methanol and 1 mole of tributyrate to form 3 moles of fatty acid methyl ester and 1 mole of glycerol [51]. The transesterification reaction is as follows:

$$\text{TBT} + 3\,\text{MeOH} \rightarrow \text{Gly} + 3\,\text{Methyl ester} \tag{4}$$
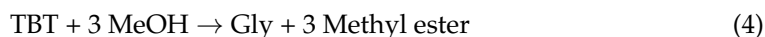
The kinetic model used in this work is based on the following assumptions:

(1) The reaction does not depend on the methanol concentration (due to it being an excess reagent), and as such, the reaction could be fitted well with pseudo-first-order rate law [51].
(2) The production of intermediate species is negligible.

$$\text{Rate} = -\text{r} = \frac{-\,\text{d}\,[\text{TBT}]}{\text{dt}} = \text{k}\,[\text{TBT}][\text{MeOH}]^3 \tag{5}$$

Based on the assumption:

$$-\text{r} = \frac{-\,\text{d}\,[\text{TBT}]}{\text{dt}} = \text{k}_{\text{TBT}} \tag{6}$$

After the integration of the Equation (6):

$$\ln\frac{[\text{TBT}]\text{o}}{[\text{TBT}]} = \text{k}_{\text{TBT}}\,.\text{t} \tag{7}$$

where $[\text{TBT}]_\text{o}$ is the initial concentration of tributyrate, $[\text{TBT}]$ is the tributyrate concentration after time t and k_{TBT} is the pseudo first order rate constant.

A plot of $\ln\frac{[\text{TBT}]\text{o}}{[\text{TBT}]}$ as a function of time is shown in Figure 10a. Table 4 shows the reaction rate constants at different reaction temperatures. The data presented in Table 4 demonstrate that the reaction rates constant '*ka*' for the CaO/ZnCo$_2$O$_4$-20 and CaO catalysts

were similar and higher than those of the other synthesized catalysts. The activation energy was calculated through the Arrhenius equation:

$$\ln k = \ln A - \frac{E_a}{RT} \tag{8}$$

where '*k*' is the reaction constant, 'A' is the frequency or preexponential factor, 'E_a' is the activation energy of the reaction, *R* is the gas constant and *T* is the absolute temperature [52]. The plot between $\ln k$ and $1/T$ (Figure 10b) was used to determine the activation energy. The experimental data obtained using $CaO/ZnCo_2O_4$-20 and CaO catalysts clearly demonstrate that the reaction followed pseudo first-order kinetics.
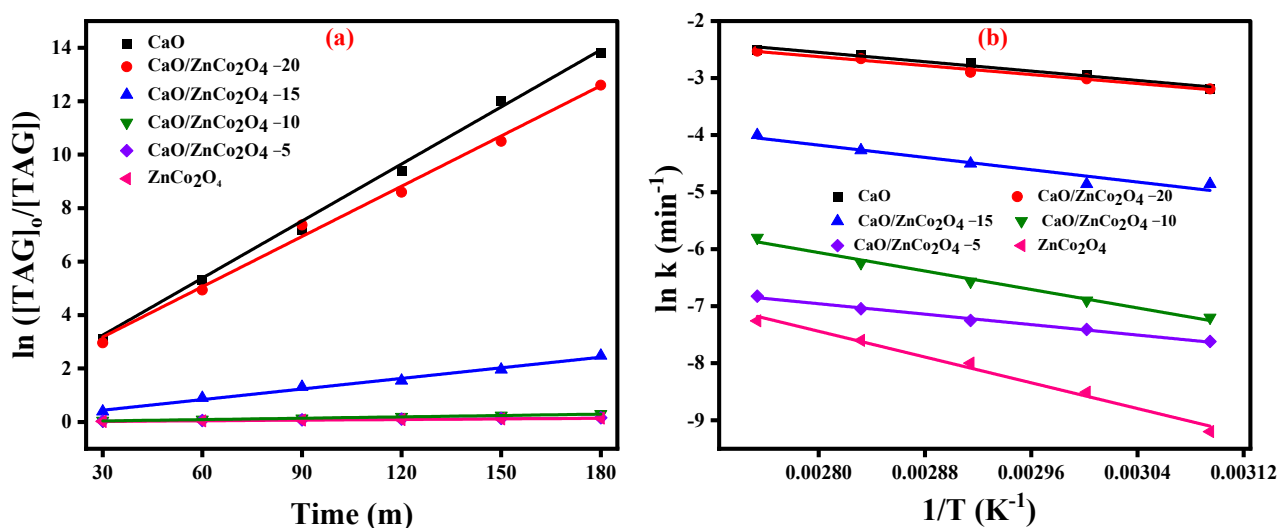

Figure 10. (**a**) Pseudo first–order reaction plot for the transesterification reaction of all the catalysts at 80 °C, (**b**) Arrhenius plots for all the catalysts.

Table 4. Reaction rate constant and activation energy over different catalysts at different reaction temperatures.

Catalyst	Reaction Rate Constant (*k*)						E_a kJ mol^{-1}
	40 °C	50 °C	60 °C	70 °C	80 °C	90 °C	
CaO	34×10^{-3}	41×10^{-3}	52×10^{-3}	64×10^{-3}	75×10^{-3}	82×10^{-3}	17
$ZnCo_2O_4$	0.07×10^{-3}	0.1×10^{-3}	0.2×10^{-3}	0.4×10^{-3}	0.5×10^{-3}	0.7×10^{-3}	48
$CaO/ZnCo_2O_4$-20	32×10^{-3}	41×10^{-3}	49×10^{-3}	55×10^{-3}	70×10^{-3}	79×10^{-3}	16
$CaO/ZnCo_2O_4$-15	2×10^{-3}	7×10^{-3}	9×10^{-3}	11×10^{-3}	14×10^{-3}	18×10^{-3}	22
$CaO/ZnCo_2O_4$-10	0.3×10^{-3}	0.7×10^{-3}	1×10^{-3}	1.4×10^{-3}	1.7×10^{-3}	4×10^{-3}	34
$CaO/ZnCo_2O_4$-5	0.1×10^{-3}	0.3×10^{-3}	0.4×10^{-3}	0.6×10^{-3}	1×10^{-3}	1.6×10^{-3}	36

The catalytic transesterification activity and characterization results indicated that CaO nanoparticles are the major active phase for the transesterification reaction; however, their stability was poor during the reaction, and the presence of $ZnCo_2O_4$ nanoparticles as a catalyst carrier in the $CaO/ZnCo_2O_4$-20 composite offered superior transesterification catalytic activity with added stability. The HRTEM results clearly indicated the existence of coalescence between the CaO and $ZnCo_2O_4$-particles. In addition, the $CaO/ZnCo_2O_4$-20 nanocomposite catalyst had high surface area and pore diameters with a greater number of strong basic sites; thus, the $CaO/ZnCo_2O_4$-20 composite exhibited the highest catalytic performance.

## 3. Materials and Methods

3.1. Materials

Zinc nitrate hexahydrate and cobalt nitrate hexahydrate were obtained from Sigma-Aldrich, St. Louis, MO, USA. Calcium chloride, sodium hydroxide were obtained from BDH Limited, Poole, England. Pure urea was obtained from Loba Chemie Pvt. Ltd., Mumbai, India. Ethanol was obtained from Fisher Scientific, Waltham, MA, USA. All chemicals were used as received.

3.2. Synthesis of Nanosized Materials

3.2.1. Synthesis of $ZnCo_2O_4$ Spinel

The $ZnCo_2O_4$ spinel was prepared by a co-precipitation followed by hydrothermal method (Scheme 1). In a typical synthesis, one mmol of $Zn(NO_3)_2 \cdot 6H_2O$ was mixed with two mmol of $Co(NO_3)_2 \cdot 6H_2O$, which was dissolved in 50 mL of deionized water under vigorous stirring. Then, 60 mmol of urea was dissolved in 100 mL of deionized water and added to the above solution to maintain the pH at around 11 under constant stirring. Stirring continued for 30 min to obtain a homogeneous precipitate. The obtained precipitate was placed in a Teflon-lined stainless-steel autoclave and subjected to hydrothermal treatment at 180 °C for 6 h. Then, the obtained cake was filtered and washed five times with deionized water and ethanol, before being dried in an oven at 60 °C for 6 h. The dried cake was calcined at 400 °C for 3 h in air at a heating rate of 3 °C/min.
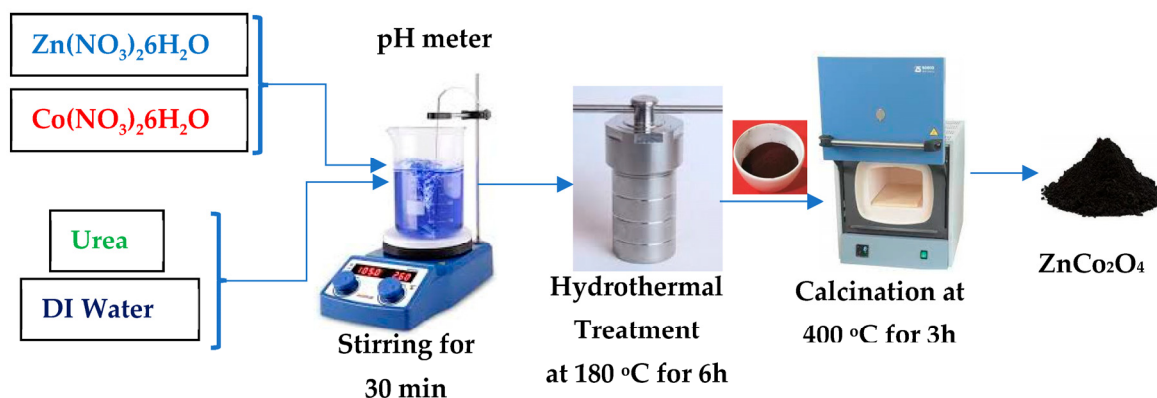
Scheme 1. Schematic representation of the synthesis of $ZnCo_2O_4$ spinel.

3.2.2. Synthesis of Calcium Oxide

Initially, $Ca(OH)_2$ was synthesized by dropwise addition of 1 M of NaOH solution to 100 mL of 0.5 M $CaCl_2$ solution under constant stirring at 80 °C, during which the pH was maintained at 11. At the end of the precipitation process, the resultant precipitate was collected and washed five times with distilled water until a pH of 7 was reached. Then, the obtained cake was dried in an oven at 60 °C for 12 h and then calcinated at 650 °C for 2 h under a N_2 atmosphere at a heating rate of 5 °C/min to obtain CaO powder.

3.2.3. Synthesis of $CaO/ZnCo_2O_4$ Nanocomposites

The $CaO/ZnCo_2O_4$ nanocomposites were prepared via a mechanochemical method by varying the CaO weight percent (5–25%). For the synthesis of the sample with different compositions, a suitable amount of $ZnCo_2O_4$ was mixed with a desirable amount of CaO and the prepared mixed powder was ground for 40 min using an agate mortar. Then, it was calcined at 300 °C for 4 h.

3.3. Material Characterization

The crystallographic structures of all prepared solid samples were characterized by X-ray diffraction using a Bruker diffractometer (Brucker D8 Advance, Karlsruhe, Germany)

equipped with Cu Kα (λ = 1.5405 Å) and a monochromator at 40 kV and 40 mA, in the 2θ range of 5°–80°. The Scherrer equation was used, i.e., d (nm) = $\frac{0.9 \times \lambda}{B \times Cos(\theta)}$, where d is the average crystallite size of the samples under investigation, λ is the wavelength of the radiation employed, 0.89 is the Scherrer constant, B is the full width at half maximum (FWHM) of diffraction peak and θ is the Bragg diffraction angle. The HRTEM images of the samples were obtained using a FEI Tecnai G2 F30 TEM microscope (Portland, OR, USA) in Bright Field imaging mode. The FT-IR spectra of the materials were obtained using a PerkinElmer FT-IR spectrometer (Waltham, MA, USA). The BET surface area, total pore volume and pore radius of different catalysts were determined from the results of N_2 physisorption performed at −196 °C using a Quantachrome Autosorb-iQ instrument (Boynton Beach, FL, USA) after degassing the samples at 200 °C for 5 h. The surface elemental compositions of the samples were analyzed by X-ray photoelectron spectroscopy utilizing a Thermo-Fisher scientific (Waltham, MA, USA) with monochromatic X-rays of Al Kα radiation at a size of 400 μm and a pressure of 10^{-9} mbar. A full-pass energy spectrum of 200 eV and in a narrow 50 eV band was applied. The binding energy of the transverse carbon line (C *1s*) was used for calibration, and the positions of the peaks were corrected relative to the C *1s* signal position. The CO_2-TPD patterns of the catalysts were obtained using a Chembet-3000 (Quantachrome, Boynton Beach, FL, USA) instrument. The sample was heated at 120 °C under helium for 1 h to remove the physically adsorbed water. Then, it was cooled to 30 °C and exposed to CO_2 gas for 1 h. Next, the sample was purged by flowing helium gas for 30 min, and then the temperature was increased from 25 °C to 900 °C at a rate of 10 °C/min. The NMR spectra were recorded at 298 K on a Bruker Avance III 400 (9.4 T, 400.13 MHz for ^{1}H, 100.62 MHz for ^{13}C) spectrometer (Bruker, Billerica, MA, USA) with a 5mm BBFO probe. Chemical shifts (δ in ppm) were relative to internal standard DMSO-d6 (δ 2.50) for ^{1}H NMR.

3.4. Transesterification of Tributyrin with Methanol

Transesterification was carried out in a 100 mL, three-necked round-bottomed flask with a reflux condenser and heated in a precisely controlled oil bath under N_2. In a typical run, 1 mmol of tributyrin (TBT) was added to 12 mmol of methanol. Then, a calculated amount of catalyst (5.0 wt.% relative to tributyrate weight) was added to the reaction mixture. The moment of adding the catalyst was regarded as the initial reaction time. The liquid samples were withdrawn periodically to determine the product distribution using a Shimadzu GC17A gas chromatograph integrated with a DB-1 capillary column and flame ionization detector. The following equations were used to determine the % conversion of tributyrin and % selectivity to the methyl butyrate [53]

$$\% \text{ Conversion of TBT } = \frac{[\text{TBT}]_{t=0} - [\text{TBT}]_t}{[\text{TBT}]_{t=0}} \times 100 \tag{9}$$

$$\% \text{ Selectivity of product } = \frac{[\text{Methyl butyrate}]_t}{3 \times [\text{TBT}]_{t=0}} \times 100 \tag{10}$$

4. Conclusions

CaO/$ZnCo_2O_4$ nanocomposite catalysts were successfully prepared via a simple mechanochemical method. They exhibited better catalytic performance in the production of biodiesel from tributyrate. A methyl ester yield of 98% was achieved over the CaO/$ZnCo_2O_4$-20 composite catalyst under the optimum reaction conditions. In addition, the nanocomposite catalyst could be reused up to five times with good activity. The excellent performance and stability of the CaO/$ZnCo_2O_4$-20 composite catalyst for the transesterification reaction were possibly due to the existence of coalescence between the CaO and $ZnCo_2O_4$-20 particles. Kinetic studies revealed that the reaction following the pseudo first-order kinetics and the number of highly basic sites in the composite catalysts were key factors affecting the catalytic performance in the transesterification reaction. These

results indicate that $ZnCo_2O_4$ spinel can be utilized as a support for the active CaO nanoparticles to develop efficient and stable heterogeneous catalysts for biodiesel production.

References

1. Acosta, P.I.; Campedelli, R.R.; Correa, E.L.; Bazani, H.A.; Nishida, E.N.; Souza, B.S.; Mora, J.R. Efficient production of biodiesel by using a highly active calcium oxide prepared in presence of pectin as heterogeneous catalyst. *Fuel* **2020**, *271*, 117651. [CrossRef]
2. Elias, S.; Rabiu, A.M.; Okeleye, B.I.; Okudoh, V.; Oyekola, O. Bifunctional Heterogeneous Catalyst for Biodiesel Production from Waste Vegetable Oil. *Appl. Sci.* **2020**, *10*, 3153. [CrossRef]
3. Sebestyén, V. Renewable and Sustainable Energy Reviews: Environmental impact networks of renewable energy power plants. *Renew. Sustain. Energy Rev.* **2021**, *151*, 111626. [CrossRef]
4. Ahmad, S.; Chaudhary, S.; Pathak, V.V.; Kothari, R.; Tyagi, V. Optimization of direct transesterification of Chlorella pyrenoidosa catalyzed by waste egg shell based heterogenous nano-CaO catalyst. *Renew. Energy* **2020**, *160*, 86–97. [CrossRef]
5. Sayed, M.R.; Abukhadra, M.R.; Ahmed, S.A.; Shaban, M.; Javed, U.; Betiha, M.A.; Shim, J.-J.; Rabie, A.M. Synthesis of advanced MgAl-LDH based geopolymer as a potential catalyst in the conversion of waste sunflower oil into biodiesel: Response surface studies. *Fuel* **2020**, *282*, 118865. [CrossRef]
6. Warkhade, G.S.; Babu, A.V. Experimental investigations on the feasibility of higher blends of biodiesel in variable compression ratio diesel engine. *Int. J. Ambient. Energy* **2020**, *41*, 1617–1627. [CrossRef]
7. Bhatia, S.K.; Bhatia, R.K.; Jeon, J.-M.; Pugazhendhi, A.; Awasthi, M.K.; Kumar, D.; Kumar, G.; Yoon, J.-J.; Yang, Y.-H. An overview on advancements in biobased transesterification methods for biodiesel production: Oil resources, extraction, biocatalysts, and process intensification technologies. *Fuel* **2021**, *285*, 119117. [CrossRef]
8. Ferreira, R.; Menezes Passos, R.; Sampaio, K.; Batista, E.A.C.; Sousa Barros Ferreira, R.; Menezes dos Passos, R.; Araujo Sampaio, K.; Augusto Caldas Batista, E. Heterogeneous Catalysts for Biodiesel Production: A Review. *Food Public Health* **2019**, *9*, 125–137. [CrossRef]
9. Abdullah, B.; Muhammad, S.A.F.S.; Shokravi, Z.; Ismail, S.; Kassim, K.A.; Mahmood, A.N.; Aziz, M.A. Fourth generation biofuel: A review on risks and mitigation strategies. *Renew. Sustain. Energy Rev.* **2019**, *107*, 37–50. [CrossRef]
10. Kumar, P.; Aslam, M.; Singh, N.; Mittal, S.; Bansal, A.; Jha, M.K.; Sarma, A.K. Characterization, activity and process optimization with a biomass-based thermal power plant's fly ash as a potential catalyst for biodiesel production. *RSC Adv.* **2015**, *5*, 9946–9954. [CrossRef]
11. Malpani, M.; Varma, A.K.; Mondal, P. Production of bio-oil from algal biomass and its upgradation to biodiesel using CaO-based heterogeneous catalysts. *Int. J. Green Energy* **2016**, *13*, 969–976. [CrossRef]
12. Chakraborty, R.; Chatterjee, S.; Mukhopadhyay, P.; Barman, S. Progresses in Waste Biomass Derived Catalyst for Production of Biodiesel and Bioethanol: A Review. *Procedia Environ. Sci.* **2016**, *35*, 546–554. [CrossRef]
13. Lim, S.; Ling, P.Y.; Jun, L.W. Synthesis and characterisation of carbon-based solid acid catalyst from Jatropha biomass for biodiesel production. *AIP Conf. Proc.* **2019**, *2157*, 020052. [CrossRef]
14. Delgado-Mellado, N.; Ayuso, M.; Villar-Chavero, M.M.; García, J.; Rodríguez, F. Ecotoxity evaluation towards Vibrio fischeri of imidazolium- and pyridinium-based ionic liquids for their use in separation processes. *SN Appl. Sci.* **2019**, *1*, 896. [CrossRef]
15. Ling, J.S.J.; Tan, Y.H.; Mubarak, N.M.; Kansedo, J.; Saptoro, A.; Nolasco-Hipolito, C. A review of heterogeneous calcium oxide based catalyst from waste for biodiesel synthesis. *SN Appl. Sci.* **2019**, *1*, 810. [CrossRef]

16. Katre, G.; Raskar, S.; Zinjarde, S.; Kumar, V.R.; Kulkarni, B.; RaviKumar, A. Optimization of the insitu transesterification step for biodiesel production using biomass of Yarrowia lipolytica NCIM 3589 grown on waste cooking oil. *Energy* **2018**, *142*, 944–952. [CrossRef]

17. Kaur, M.; Malhotra, R.; Ali, A. Tungsten supported Ti/SiO$_2$ nanoflowers as reusable heterogeneous catalyst for biodiesel production. *Renew. Energy* **2018**, *116*, 109–119. [CrossRef]

18. Kusiak, A.; Zhang, Z.; Verma, A. Prediction, operations, and condition monitoring in wind energy. *Energy* **2013**, *60*, 1–12. [CrossRef]

19. Guariento, A.H.; Furtado, K.S.; de Conti, A.; Campos, A.; Purgatto, E.; Carrilho, J.; Shinohara, E.M.G.; Tryndyak, V.; Han, T.; Fuscoe, J.C.; et al. Transcriptomic responses provide a new mechanistic basis for the chemopreventive effects of folic acid and tributyrin in rat liver carcinogenesis. *Int. J. Cancer* **2014**, *135*, 7–18. [CrossRef]

20. Odude, V.O.; Adesina, A.J.; Oyetunde, O.O.; Adeyemi, O.O.; Ishola, N.B.; Etim, A.O.; Betiku, E. Application of Agricultural Waste-Based Catalysts to Transesterification of Esterified Palm Kernel Oil into Biodiesel: A Case of Banana Fruit Peel Versus Cocoa Pod Husk. *Waste Biomass Valorization* **2019**, *10*, 877–888. [CrossRef]

21. Gohain, M.; Devi, A.; Deka, D. Musa balbisiana Colla peel as highly effective renewable heterogeneous base catalyst for biodiesel production. *Ind. Crop. Prod.* **2017**, *109*, 8–18. [CrossRef]

22. de Lima, A.L.; Ronconi, C.M.; Mota, C.J.A. Heterogeneous basic catalysts for biodiesel production. *Catal. Sci. Technol.* **2016**, *6*, 2877–2891. [CrossRef]

23. Li, Z.; Ding, S.; Chen, C.; Qu, S.; Du, L.; Lu, J.; Ding, J. Recyclable Li/NaY zeolite as a heterogeneous alkaline catalyst for biodiesel production: Process optimization and kinetics study. *Energy Convers. Manag.* **2019**, *192*, 335–345. [CrossRef]

24. Sulaiman, N.F.; Hashim, A.N.N.; Toemen, S.; Rosid, S.J.M.; Mokhtar, W.N.A.W.; Nadarajan, R.; Abu Bakar, W.A.W. Biodiesel production from refined used cooking oil using co-metal oxide catalyzed transesterification. *Renew. Energy* **2020**, *153*, 1–11. [CrossRef]

25. Banković–Ilić, I.B.; Miladinović, M.R.; Stamenković, O.S.; Veljković, V.B. Application of nano CaO–based catalysts in biodiesel synthesis. *Renew. Sustain. Energy Rev.* **2017**, *72*, 746–760. [CrossRef]

26. Bharadwaj, A.S.; Singh, M.; Niju, S.; Begum, K.M.S.; Anantharaman, N. Biodiesel production from rubber seed oil using calcium oxide derived from eggshell as catalyst—Optimization and modeling studies. *Green Process. Synth.* **2019**, *8*, 430–442. [CrossRef]

27. Thitsartarn, W.; Kawi, S. An active and stable CaO–CeO$_2$ catalyst for transesterification of oil to biodiesel. *Green Chem.* **2011**, *13*, 3423–3430. [CrossRef]

28. Yu, X.; Wen, Z.; Li, H.; Tu, S.-T.; Yan, J. Transesterification of Pistacia chinensis oil for biodiesel catalyzed by CaO–CeO$_2$ mixed oxides. *Fuel* **2011**, *90*, 1868–1874. [CrossRef]

29. Vozniuk, O.; Tabanelli, T.; Tanchoux, N.; Millet, J.-M.M.; Albonetti, S.; Di Renzo, F.; Cavani, F. Mixed-Oxide Catalysts with Spinel Structure for the Valorization of Biomass: The Chemical-Loop Reforming of Bioethanol. *Catalysts* **2018**, *8*, 332. [CrossRef]

30. Wei, R.; Bu, X.; Gao, W.; Villaos, R.A.B.; Macam, G.; Huang, Z.-Q.; Lan, C.; Chuang, F.-C.; Qu, Y.; Ho, J.C. Engineering Surface Structure of Spinel Oxides via High-Valent Vanadium Doping for Remarkably Enhanced Electrocatalytic Oxygen Evolution Reaction. *ACS Appl. Mater. Interfaces* **2019**, *11*, 33012–33021. [CrossRef]

31. Liu, Y.; Zhang, P.; Fan, M.; Jiang, P. Biodiesel production from soybean oil catalyzed by magnetic nanoparticle MgFe$_2$O$_4$@CaO. *Fuel* **2016**, *164*, 314–321. [CrossRef]

32. Galmiz, O.; Stupavska, M.; Wulff, H.; Kersten, H.; Brablec, A.; Cernak, M. Deposition of Zn-containing films using atmospheric pressure plasma jet. *Open Chem.* **2015**, *13*, 198–203. [CrossRef]

33. Xu, J.; He, L.; Wang, Y.; Zhang, C.; Zhang, Y. Preparation of bi-component ZnO/ZnCo$_2$O$_4$ nanocomposites with improved electrochemical performance as anode materials for lithium-ion batteries. *Electrochim. Acta* **2016**, *191*, 417–425. [CrossRef]

34. Fu, J.-X.; Wong, W.-T.; Liu, W.-R. Temperature effects on a nano-porous ZnCo$_2$O$_4$ anode with excellent capability for Li-ion batteries. *RSC Adv.* **2015**, *5*, 75838–75845. [CrossRef]

35. Xiao, X.; Peng, B.; Cai, L.; Zhang, X.; Liu, S.; Wang, Y. The high efficient catalytic properties for thermal decomposition of ammonium perchlorate using mesoporous ZnCo$_2$O$_4$ rods synthesized by oxalate co-precipitation method. *Sci. Rep.* **2018**, *8*, 7571. [CrossRef]

36. Priya, M.; Premkumar, V.; Vasantharani, P.; Sivakumar, G. Structural and electrochemical properties of ZnCo$_2$O$_4$ nanoparticles synthesized by hydrothermal method. *Vacuum* **2019**, *167*, 307–312. [CrossRef]

37. Mirghiasi, Z.; Bakhtiari, F.; Darezereshki, E.; Esmaeilzadeh, E. Preparation and characterization of CaO nanoparticles from Ca(OH)$_2$ by direct thermal decomposition method. *J. Ind. Eng. Chem.* **2014**, *20*, 113–117. [CrossRef]

38. Roy, A.; Bhattacharya, J. Microwave-assisted synthesis and characterization of CaO nanoparticles. *Int. J. Nanosci.* **2011**, *10*, 413–418. [CrossRef]

39. Xiao, X.; Wang, G.; Zhang, M.; Wang, Z.; Zhao, R.; Wang, Y. Electrochemical performance of mesoporous ZnCo$_2$O$_4$ nanosheets as an electrode material for supercapacitor. *Ionics* **2018**, *24*, 2435–2443. [CrossRef]

40. Hao, S.; Zhang, B.; Ball, S.; Copley, M.; Xu, Z.; Srinivasan, M.; Zhou, K.; Mhaisalkar, S.; Huang, Y. Synthesis of multimodal porous ZnCo$_2$O$_4$ and its electrochemical properties as an anode material for lithium ion batteries. *J. Power Sources* **2015**, *294*, 112–119. [CrossRef]

41. Abouzir, E.; Elansary, M.; Belaiche, M.; Jaziri, H. Magnetic and structural properties of single-phase Gd^{3+}-substituted Co–Mg ferrite nanoparticles. *RSC Adv.* **2020**, *10*, 11244–11256. [CrossRef] [PubMed]

42. Li, J.; Wang, J.; Wexler, D.; Shi, D.; Liang, J.; Liu, H.; Xiong, S.; Qian, Y. Simple synthesis of yolk-shelled $ZnCo_2O_4$ microspheres towards enhancing the electrochemical performance of lithium-ion batteries in conjunction with a sodium carboxymethyl cellulose binder. *J. Mater. Chem. A* **2013**, *1*, 15292–15299. [CrossRef]

43. Zhu, J.; Gao, Q. Mesoporous MCo_2O_4 (M = Cu, Mn and Ni) spinels: Structural replication, characterization and catalytic application in CO oxidation. *Microporous Mesoporous Mater.* **2009**, *124*, 144–152. [CrossRef]

44. Wu, H.; Qin, M.; Zhang, L. $NiCo_2O_4$ constructed by different dimensions of building blocks with superior electromagnetic wave absorption performance. *Compos. Part B Eng.* **2020**, *182*, 107620. [CrossRef]

45. Li, X.; Jiang, L.; Zhou, C.; Liu, J.; Zeng, H. Integrating large specific surface area and high conductivity in hydrogenated $NiCo_2O_4$ double-shell hollow spheres to improve supercapacitors. *NPG Asia Mater.* **2015**, *7*, e165. [CrossRef]

46. Zhang, P.; Han, Q.; Fan, M.; Jiang, P. Magnetic solid base catalyst $CaO/CoFe_2O_4$ for biodiesel production: Influence of basicity and wettability of the catalyst in catalytic performance. *Appl. Surf. Sci.* **2014**, *317*, 1125–1130. [CrossRef]

47. Bai, L.; Tajikfar, A.; Tamjidi, S.; Foroutan, R.; Esmaeili, H. Synthesis of $MnFe_2O_4$@graphene oxide catalyst for biodiesel production from waste edible oil. *Renew. Energy* **2021**, *170*, 426–437. [CrossRef]

48. Al-Shammari, B.; Alsulami, Q.A.; Narasimharao, K. Lanthanum Exchanged Keggin Structured Heteropoly Compounds for Biodiesel Production. *Catalysts* **2019**, *9*, 979. [CrossRef]

49. Zhang, N.; Xue, H.; Hu, R. The activity and stability of CeO_2@CaO catalysts for the production of biodiesel. *RSC Adv.* **2018**, *8*, 32922–32929. [CrossRef]

50. Ullah, Z.; Bustam, M.A.; Man, Z.; Khan, A.S.; Muhammad, N.; Sarwono, A. Preparation and kinetics study of biodiesel production from waste cooking oil using new functionalized ionic liquids as catalysts. *Renew. Energy* **2017**, *114*, 755–765. [CrossRef]

51. Feyzi, M.; Norouzi, L. Preparation and kinetic study of magnetic Ca/Fe_3O_4@SiO_2 nanocatalysts for biodiesel production. *Renew. Energy* **2016**, *94*, 579–586. [CrossRef]

52. Ma, Y.; Wang, Q.; Sun, X.; Wu, C.; Gao, Z. Kinetics studies of biodiesel production from waste cooking oil using $FeCl_3$-modified resin as heterogeneous catalyst. *Renew. Energy* **2017**, *107*, 522–530. [CrossRef]

53. Rabee, A.I.M.; Manayil, J.C.; Isaacs, M.A.; Parlett, C.M.A.; Durndell, L.J.; Zaki, M.I.; Lee, A.F.; Wilson, K. On the Impact of the Preparation Method on the Surface Basicity of Mg–Zr Mixed Oxide Catalysts for Tributyrin Transesterification. *Catalysts* **2018**, *8*, 228. [CrossRef]